ATOMS : ALMA Three-millimeter Observations of Massive Star-forming regions - VIII. A search for hot cores by using C2H5CN, CH3OCHO, and CH3OH lines

Qin, Sheng-Li

2022-02-21

Qin , S-L , Liu , T , Liu , X , Goldsmith , P F , Li , D , Zhang , Q , Liu , H-L , Wu , Y , Bronfman , L , Juvela , M , Lee , C W , Garay , G , Zhang , Y , He , J , Hsu , S-Y , Shen , Z-Q , Lee , J-E , Wang , K , Tang , N , Tang , M , Zhang , C , Yue , Y , Xue , Q , Li , S , Peng , Y , Dutta , S , Ge , J , Xu , F , Chen , L-F , Baug , T , Dewangan , L & Tej , A 2022 , ' ATOMS : ALMA Three-millimeter Observations of Massive Star-forming regions - VIII. A search for hot cores by using C2H5CN, CH3OCHO, and CH3OH lines ' , Monthly Notices of the Royal Astronomical Society , vol. 511 , no. 3 , pp. 3463-3476 . https://doi.org/10.1093/mnras/stac219

http://hdl.handle.net/10138/352552
https://doi.org/10.1093/mnras/stac219

unspecified
publishedVersion

Monthly Notices of the ROYAL ASTRONOMICAL SOCIETY

MNRAS **511,** 3463–3476 (2022) https://doi.org/10.1093/mnras/stac219
Advance Access publication 2022 January 29

ATOMS: ALMA Three-millimeter Observations of Massive Star-forming regions – VIII. A search for hot cores by using C_2H_5CN, CH_3OCHO, and CH_3OH lines

Sheng-Li Qin,[1★] Tie Liu,[2★] Xunchuan Liu,[2] Paul F. Goldsmith,[3] Di Li,[4,5,6] Qizhou Zhang,[7] Hong-Li Liu,[1] Yuefang Wu,[8] Leonardo Bronfman,[9] Mika Juvela,[10] Chang Won Lee,[11,12] Guido Garay,[9] Yong Zhang,[13] Jinhua He,[9,14,15] Shih-Ying Hsu,[16] Zhi-Qiang Shen,[2] Jeong-Eun Lee,[17] Ke Wang,[18] Ningyu Tang,[19] Mengyao Tang,[20] Chao Zhang,[21] Yinghua Yue,[1] Qiaowei Xue,[1] Shanghuo Li,[11] Yaping Peng,[22] Somnath Dutta,[16] Jixing Ge,[15] Fengwei Xu,[8,18] Long-Fei Chen,[4] Tapas Baug,[23] Lokesh Dewangan[24] and Anandmayee Tej[25]

Affiliations are listed at the end of the paper

Accepted 2022 January 21. Received 2022 January 21; in original form 2022 January 5

ABSTRACT

Hot cores characterized by rich lines of complex organic molecules are considered as ideal sites for investigating the physical and chemical environments of massive star formation. We present a search for hot cores by using typical nitrogen- and oxygen-bearing complex organic molecules (C_2H_5CN, CH_3OCHO, and CH_3OH), based on ALMA Three-millimeter Observations of Massive Star-forming regions (ATOMS). The angular resolutions and line sensitivities of the ALMA observations are better than 2 arcsec and 10 mJy beam^{-1}, respectively. A total of 60 hot cores are identified with 45 being newly detected, in which the complex organic molecules have high gas temperatures (> 100 K) and hot cores have small source sizes (< 0.1 pc). So far, this is the largest sample of hot cores observed with similar angular resolution and spectral coverage. The observations have also shown nitrogen and oxygen differentiation in both line emission and gas distribution in 29 hot cores. Column densities of CH_3OH and CH_3OCHO increase as rotation temperatures rise. The column density of CH_3OCHO correlates tightly with that of CH_3OH. The pathways for production of different species are discussed. Based on the spatial position difference between hot cores and ultracompact H II (UC H II) regions, we conclude that 24 hot cores are externally heated, while the other hot cores are internally heated. The observations presented here will potentially help establish a hot core template for studying massive star formation and astrochemistry.

Key words: astrochemistry – stars: formation – ISM: molecules.

1 INTRODUCTION

Massive stars play an important role in shaping structure and evolution of galaxies, but also can affect star and planet formation. They also are dominant sources of heavy elements and ultraviolet radiation (see Zinnecker & Yorke 2007, and references therein). How massive stars form is not yet well understood. During massive star formation processes, the hot core phase is particularly important since hot cores may trace the physical and chemical environments where massive stars are born. When clouds collapse to form massive stars, the material surrounding these objects is heated up, leading to the formation of hot cores with rich chemistry.

Hot cores are characterized by rich line emission from complex organic molecules (COMs) with higher gas temperatures (> 100 K) and smaller source sizes (<0.1 pc; e.g. Kurtz et al. 2000; Cesaroni 2005). Of the detected 250 molecular species[1] (see also McGuire 2021), most of COMs, as well as simple molecules, are frequently observed in hot cores. Different molecules are used for probing different physical components at different scales (van Dishoeck & Blake 1998; Jørgensen, Belloche & Garrod 2021; Tychoniec et al. 2021). Especially, COMs are thought to play an important role in prebiotic chemistry, which may be linked to the origin of life (e.g. Herbst & van Dishoeck 2009; Ceccarelli et al. 2017). Therefore, observations towards hot cores are crucial in the study of massive star formation and astrochemistry.

Hot cores have been observed towards individual cases and large samples of sources by single-dish telescopes (Schilke et al. 1997, 2001, 2006; Gibb et al. 2000a; van der Tak, van Dishoeck & Caselli 2000; Bisschop et al. 2007; Fontani et al. 2007; Bergin et al. 2010; Belloche et al. 2013; Halfen, Ilyushin & Ziurys 2013; Crockett et al. 2014; Neill et al. 2014; Suzuki et al. 2016, 2018; Widicus Weaver

★ E-mail: qin@ynu.edu.cn (SLQ); liutie@shao.ac.cn (TL)

[1] https://cdms.astro.uni-koeln.de/classic/molecules

et al. 2017; Ospina-Zamudio et al. 2018; Hernández-Hernández et al. 2019; Coletta et al. 2020; Li et al. 2020; Möller et al. 2021; Xie et al. 2021). Due to small source sizes of hot cores, single-dish observations suffer from beam dilution and sample the emission from both hot cores and surrounding cold envelopes. The millimetre/submillimetre interferometric arrays (e.g. SMA, NOEMA, and ALMA) offer larger bandwidth, higher spatial resolution, and increased sensitivity, which have promoted the hot core observations greatly, but mainly focused on individual sources or small samples (Liu, Mehringer & Snyder 2001; Liu et al. 2002; Remijan et al. 2003, 2004; Qin et al. 2008, 2010, 2015; Beuther et al. 2005, 2009; Sánchez-Monge et al. 2010, 2014; Rathborne et al. 2011; Zapata, Schmid-Burgk & Menten 2011; Sakai et al. 2013, 2018; Hernández-Hernández et al. 2014; Wu, Liu & Qin 2014; Belloche et al. 2016, 2019; Brogan et al. 2016; Müller et al. 2016; Rong et al. 2016; Bonfand et al. 2017; Orozco-Aguilera et al. 2017; Pagani et al. 2017; Palau et al. 2017; Rivilla et al. 2017; Ahmadi et al. 2018; Guzmán et al. 2018; Tercero et al. 2018; Wong & An 2018; Bøgelund et al. 2019; Csengeri et al. 2019; Luo et al. 2019; Peng et al. 2019; Xue et al. 2019; Mottram et al. 2020; Ligterink et al. 2020; Taniguchi et al. 2020; Fuente et al. 2021; Law et al. 2021; van der Walt et al. 2021). Since these observations were made with different spatial resolution and spectral setup, it is difficult to make a comparison. More recently, a large sample including 18 well-known high-mass star-forming regions was observed by the NOEMA with the same spectral setup, suggesting that most molecules are destroyed in evolved cores having less emission lines (Gieser et al. 2021). Of the detected hot cores, a few show chemical differentiation between nitrogen- and oxygen-bearing COMs (e.g. Wyrowski et al. 1999; Remijan et al. 2004; Kalenskii & Johansson 2010; Qin et al. 2010, 2015; Feng et al. 2015; Jiménez-Serra et al. 2012; Allen et al. 2017; Mills et al. 2018; Suzuki et al. 2018; Csengeri et al. 2019; Gieser et al. 2019; Lee et al. 2019). Chemical differentiation and heating mechanism are still long-standing problems due to a lack of large sample and systematic observations.

The ALMA Three-millimeter Observations of Massive Star-forming regions (ATOMS) project has observed 146 massive clumps at 3 mm band with ALMA (Liu et al. 2020a,b). 90 out of a total of 453 compact dense cores have been considered as hot core candidates based on the number of emission lines (Liu et al. 2021). Hot cores are rich in COM lines. Especially, two typical nitrogen- and oxygen-bearing molecules C_2H_5CN and CH_3OCHO are frequently detected in hot cores. Spectral windows (SPWs) 7 and 8 were tuned to observe C_2H_5CN and CH_3OCHO with more than three transitions, which are suitable for identifying hot cores. Comparing with the submillimetre waveband, the lines at 3 mm have much less blending problem. Aiming to build up a large sample of hot cores, we conduct a survey using C_2H_5CN and CH_3OCHO lines based on the ATOMS continuum and line data at 3 mm band in this work. The two molecules can also be used for investigating chemical differentiation among these hot cores. The observations and data reduction are briefly described in Section 2, and the observational results including hot core identification and parameter calculation are given in Section 3. We discuss the heating mechanism and nitrogen and oxygen differentiation in Section 4. The main results and conclusions are summarized in Section 5.

2 OBSERVATIONS

The sample selection and basic observational parameters are described in Liu et al. (2020a). In brief, the ALMA band 3 observations were made towards 146 massive clumps from 2019 September to mid-November with both the Atacama Compact 7 m Array and the 12 m array (C43-2 or C43-3 configurations). The correlator setup was tuned to include eight SPWs, with six windows (SPWs 1–6) having higher spectral resolutions of ∼0.2–0.4 km s^{-1} in the lower sideband and SPWs 7 and 8 having lower spectral resolutions in the upper sideband. SPWs 7 and 8 have a broad bandwidth of 1875 MHz corresponding to a spectral resolution of ∼1.6 km s^{-1}, which were used for continuum imaging and line survey purposes. The frequencies of SPWs 7 and 8 range from 97 536 to 99 442 MHz, and from 99 470 to 101 390 MHz, respectively, covering many of COM lines. In addition to the COM lines, the H40α line at 99 023 MHz is included in SPW 7 used for H II region identification. SiO (2–1) lines at 86 847 MHz are tuned in SPW 4 for tracing shocked gas. Since hot cores have smaller source sizes and COM lines suffer from less missing flux problem, we only use the 12 m array data for identifications of COM lines and hot cores in this work. Data reduction was done using the CASA software package version 5.6 (McMullin et al. 2007). The resultant continuum image and line cubes with the 12 m array data for the 146 clumps have angular resolutions of ∼1.2–1.9 arcsec and maximum recoverable angular scales of ∼14.5–20.3 arcsec. The mean 1σ noise level is better than 10 mJy beam^{-1} per channel for lines, and 0.4 mJy beam^{-1} for continuum. Taking an angular resolution of 1.9 arcsec and 3σ level, the position accuracy of line images due to the noise is estimated to be better than 0.3 arcsec by using the formula $\Delta\theta = 0.45\,\frac{\theta_{\rm FWHM}}{\rm S/N}$ (Reid et al. 1988).

3 RESULTS

3.1 Line and hot core identifications

As stated before, 453 compact dense cores were found in 146 massive clumps (Liu et al. 2021). We have inspected the line emission of the 453 cores one by one and extracted spectra at the line-rich positions. In total, 60 line-rich cores are considered as hot core candidates. The results are in good agreement with those by Liu et al. (2021), where 54 cores were found in a statistic manner to have significant detection of at least 20 COM transitions with line intensities larger than the 3σ level. Then we use the eXtended CASA Line Analysis Software Suite (XCLASS[2]; Möller, Endres & Schilke 2017) for further line identification and parameter calculation. The XCLASS accesses the Cologne Database for Molecular Spectroscopy (Müller et al. 2001, 2005) and Jet Propulsion Laboratory molecular databases (Pickett et al. 1998). Assuming that the molecular gas satisfies the local thermodynamical equilibrium (LTE) condition, the XCLASS solves a radiative transfer equation and produces synthetic spectra for specific molecular transitions by taking the source size, beam filling factor, line profile, line blending, excitation, and opacity into account. In the XCLASS modelling, the input parameters are the source size, beam size, line velocity width, velocity offset, rotation temperature, and column density (Möller et al. 2017). In our case, we take deconvolved angular sizes of the continuum sources as source sizes, which are listed in Table 1. The velocity offsets with respect to systemic velocities of the hot cores are determined when referred to commonly detected CH_3OH line at 100.6389 GHz. Therefore, we set rotation temperatures, column densities, and velocity widths as free parameters to simulate the observed spectra. To obtain optimized rotation temperature and column density parameters, we employ Modeling and Analysis Generic Interface

[2]https://xclass.astro.uni-koeln.de/

Table 1. Physical parameters of the hot cores.

Source	RA	Dec.	θ_{source}		C_2H_5CN			CH_3OCHO		CH_3OH	
	(^{h} ^{m} ^{s})	($^\circ$ $'$ $''$)	(arcsec)	T_{rot} (K)	N (cm^{-2})	f	T_{rot} (K)	N (cm^{-2})	f	T_{rot} (K)	N (cm^{-2})
I08303−4303^S	08:32:08.68	−43:13:45.78	2.2	104 ± 16	(7.1 ± 1.0) × 10^{14}	(2.8 ± 0.4) × 10^{-3}	101 ± 9	(1.5 ± 0.2) × 10^{16}	(6.1 ± 0.1) × 10^{-2}	101	2.5 × 10^{17}
I08470−4243^S	08:48:47.79	−42:54:27.90	1.8	125 ± 18	(1.3 ± 0.2) × 10^{15}	(1.5 ± 0.3) × 10^{-3}	200 ± 30	(2.1 ± 0.2) × 10^{17}	(2.5 ± 0.1) × 10^{-1}	202 ± 32	(8.5 ± 1.1) × 10^{17}
I09018−4816	09:03:33.46	−48:28:01.69	3.4							160 ± 8	(1.9 ± 0.1) × 10^{17}
I11298−6155^E	11:32:05.59	−62:12:25.62	3.1				124 ± 6	(1.3 ± 0.3) × 10^{16}	(8.3 ± 5.3) × 10^{-2}	124	1.6 × 10^{17}
I12326−6245^{E,S}	12:35:35.09	−63:02:31.91	1.3	130 ± 32	(3.1 ± 0.2) × 10^{15}	(8.4 ± 0.5) × 10^{-3}	137 ± 33	(2.3 ± 0.2) × 10^{16}	(6.2 ± 0.6) × 10^{-2}	137	3.7 × 10^{17}
I13079−6218	13:11:13.75	−62:34:41.55	2.4	100 ± 13	(2.1 ± 0.2) × 10^{16}	(1.2 ± 0.2) × 10^{-2}	110 ± 9	(1.1 ± 0.3) × 10^{17}	(8.5 ± 2) × 10^{-2}	110	1.3 × 10^{18}
I13134−6242	13:16:43.2	−62:58:32.3	2.2	139 ± 4	(8.2 ± 0.5) × 10^{15}	(7.5 ± 0.5) × 10^{-3}	160 ± 5	(2.1 ± 0.1) × 10^{17}	(1.9 ± 0.1) × 10^{-1}	160	1.1 × 10^{18}
I13140−6226^S	13:17:15.49	−62:42:24.42	5.5	139 ± 4	(5.9 ± 0.1) × 10^{14}	(7.4 ± 0.2) × 10^{-3}	120 ± 17	(6.7 ± 0.1) × 10^{15}	(8.4 ± 0.1) × 10^{-2}	120	8.1 × 10^{16}
I13471−6120^{E,S}	13:50:41.81	−61:35:10.67	1	134 ± 8	(2.2 ± 0.5) × 10^{15}	(1.7 ± 0.4) × 10^{-3}	126 ± 10	(1.1 ± 0.2) × 10^{17}	(8.5 ± 1.3) × 10^{-2}	126	1.3 × 10^{18}
I13484−6100	13:51:58.31	−61:15:41.5	2.5	131 ± 18	(1.6 ± 0.6) × 10^{15}	(1.5 ± 0.5) × 10^{-2}				126	1.1 × 10^{17}
I14498−5856^S	14:53:42.68	−59:08:52.89	2.8	144 ± 13	(8.6 ± 0.1) × 10^{14}	(1.9 ± 0.1) × 10^{-3}	106 ± 3	(1.5 ± 0.1) × 10^{16}	(3.3 ± 0.3) × 10^{-2}	135 ± 8	(4.5 ± 0.4) × 10^{17}
I15254−5621^E	15:29:19.39	−56:31:22.34	0.8	148 ± 3	(4.2 ± 0.1) × 10^{15}	(2.3 ± 0.2) × 10^{-3}	146 ± 14	(9.2 ± 0.2) × 10^{16}	(5.2 ± 0.4) × 10^{-2}	165 ± 13	(1.8 ± 0.1) × 10^{18}
I15437−5343	15:47:32.73	−53:52:38.8	2.3	128 ± 20	(1.3 ± 0.1) × 10^{15}	(1.7 ± 0.1) × 10^{-3}	106 ± 11	(2.1 ± 0.1) × 10^{16}	(2.8 ± 0.2) × 10^{-2}	170 ± 28	(7.5 ± 0.4) × 10^{17}
I15520−5234^{E,S}	15:55:48.47	−52:43:06.75	2.9	118 ± 13	(1.6 ± 0.1) × 10^{15}	(3.6 ± 0.3) × 10^{-3}	160 ± 30	(3.7 ± 0.1) × 10^{16}	(8.4 ± 0.4) × 10^{-2}	168 ± 28	(4.4 ± 0.1) × 10^{17}
I16060−5146^{E,S}	16:09:52.64	−51:54:54.49	1.9	110 ± 5	(3 ± 0.2) × 10^{15}	(2 ± 0.1) × 10^{-2}	110 ± 22	(2.5 ± 0.2) × 10^{16}	(1.7 ± 0.2) × 10^{-1}	110	1.5 × 10^{17}
I16065−5158^{E,S}	16:10:19.99	−52:06:07.25	3.1	125 ± 15	(2 ± 0.1) × 10^{16}	(1.5 ± 0.2) × 10^{-2}	150 ± 43	(8.9 ± 0.1) × 10^{16}	(6.8 ± 0.1) × 10^{-2}	174 ± 14	(1.3 ± 0.1) × 10^{18}
I16071−5142^E	16:10:59.59	−51:50:23.37	4.2	161 ± 6	(1.1 ± 0.1) × 10^{16}	(1.1 ± 0.1) × 10^{-2}	150 ± 20	(1.1 ± 0.1) × 10^{17}	(1.1 ± 0.1) × 10^{-1}	190 ± 16	(9.8 ± 0.2) × 10^{17}
I16076−5134^{E,S}	16:11:26.59	−51:41:57.84	4.3	110 ± 18	(3.4 ± 0.2) × 10^{15}	(2 ± 0.2) × 10^{-2}	121 ± 32	(2.5 ± 0.3) × 10^{16}	(1.5 ± 0.2) × 10^{-1}	130 ± 14	(1.7 ± 0.1) × 10^{17}
I16164−5046^E	16:20:11.08	−50:53:14.75	2.8	133 ± 20	(7.4 ± 0.1) × 10^{15}	(8.1 ± 0.2) × 10^{-3}	157 ± 19	(1.2 ± 0.2) × 10^{17}	(1.3 ± 0.2) × 10^{-1}	187 ± 74	(9.1 ± 0.1) × 10^{17}
I16172−5028^{E,S}	16:21:02.97	−50:35:12.6	1.8	110 ± 32	(1.9 ± 0.3) × 10^{15}	(3.3 ± 0.5) × 10^{-3}				204 ± 18	(5.7 ± 0.1) × 10^{17}
I16272−4837c1	16:30:58.77	−48:43:53.57	2.2	220 ± 8	(4.2 ± 0.1) × 10^{16}	(1.3 ± 0.1) × 10^{-2}	230 ± 37	(8.9 ± 0.2) × 10^{17}	(2.8 ± 0.1) × 10^{-1}	240 ± 21	(3.2 ± 0.1) × 10^{18}
I16272−4837c2	16:30:58.68	−48:43:51.32	2	120 ± 3	(3.1 ± 0.1) × 10^{15}	(6.9 ± 0.1) × 10^{-3}	150 ± 9	(3.9 ± 0.1) × 10^{16}	(8.7 ± 0.1) × 10^{-2}	180 ± 6	(4.5 ± 0.1) × 10^{17}
I16272−4837c3	16:30:57.29	−48:43:39.87	2.1	103 ± 11	(2.1 ± 0.1) × 10^{15}	(6.9 ± 0.1) × 10^{-3}	123 ± 12	(3.8 ± 0.1) × 10^{15}	(8.7 ± 0.1) × 10^{-2}	123 ± 6	(2.1 ± 0.1) × 10^{17}
I16318−4724^E	16:35:33.96	−47:31:11.59	2.2	130 ± 5	(2.7 ± 0.1) × 10^{16}	(9.6 ± 0.8) × 10^{-3}	148 ± 15	(1.9 ± 0.5) × 10^{17}	(6.8 ± 0.2) × 10^{-2}	192 ± 18	(2.8 ± 0.2) × 10^{18}
I16344−4658^E	16:38:09.49	−47:04:59.73	1.7	150 ± 4	(5.5 ± 0.1) × 10^{15}	(1.1 ± 0.1) × 10^{-2}	160 ± 15	(5.2 ± 0.1) × 10^{16}	(1.1 ± 0.1) × 10^{-1}	160 ± 12	(4.8 ± 0.1) × 10^{17}
I16348−4654^{E,S}	16:38:29.65	−47:00:35.67	0.8	270 ± 13	(2 ± 0.1) × 10^{17}	(1.3 ± 0.1) × 10^{-2}	213 ± 12	(2 ± 0.1) × 10^{18}	(1.3 ± 0.1) × 10^{-1}	220 ± 12	(1.5 ± 0.1) × 10^{19}
I16351−4722^{E,S}	16:38:50.50	−47:28:00.68	1.5	121 ± 10	(5.7 ± 0.1) × 10^{15}	(7.6 ± 0.1) × 10^{-3}	150 ± 31	(6 ± 0.3) × 10^{16}	(8 ± 0.4) × 10^{-2}	150	7.5 × 10^{17}
I16458−4512^S	16:49:30.04	−45:17:44.58	1.1				120 ± 4	(2.1 ± 0.1) × 10^{16}	(1.4 ± 0.1) × 10^{-1}	120	1.5 × 10^{17}
I16484−4603	16:52:04.66	−46:08:33.85	1.3	120 ± 12	(1.7 ± 0.3) × 10^{15}	(1 ± 0.3) × 10^{-3}	127 ± 5	(6.1 ± 0.3) × 10^{16}	(3.6 ± 0.3) × 10^{-2}	151 ± 4	(1.7 ± 0.1) × 10^{18}
I16547−4247^S	16:58:17.18	−42:52:07.57	2.5	114 ± 8	(3.1 ± 0.1) × 10^{15}	(7.8 ± 0.3) × 10^{-3}	150 ± 20	(2.2 ± 0.2) × 10^{16}	(5.5 ± 0.4) × 10^{-2}	170 ± 5	(4 ± 0.1) × 10^{17}
I17008−4040	17:04:22.91	−40:44:22.91	1.7	161 ± 7	(1.6 ± 0.1) × 10^{16}	(5 ± 0.1) × 10^{-3}	150 ± 14	(2.8 ± 0.1) × 10^{17}	(8.8 ± 0.1) × 10^{-2}	180 ± 12	(3.2 ± 0.1) × 10^{18}
I17016−4124c1^E	17:05:10.97	−41:29:06.95	0.9	153 ± 6	(3.6 ± 0.1) × 10^{16}	(7.8 ± 0.1) × 10^{-3}	143 ± 14	(4.9 ± 0.1) × 10^{17}	(1.1 ± 0.1) × 10^{-1}	193 ± 14	(4.6 ± 0.1) × 10^{18}
I17016−4124c2	17:05:11.20	−41:29:07.05	1.8	101 ± 12	(5 ± 0.2) × 10^{15}	(1.7 ± 0.1) × 10^{-3}	165 ± 32	(2 ± 0.3) × 10^{17}	(6.6 ± 0.1) × 10^{-2}	180 ± 11	(3.1 ± 0.1) × 10^{18}
I17158−3901c1	17:19:20.43	−39:03:51.58	2.9	152 ± 9	(1 ± 0.1) × 10^{15}	(3.2 ± 0.4) × 10^{-3}	151 ± 12	(2.2 ± 0.2) × 10^{16}	(7.1 ± 0.5) × 10^{-2}	150 ± 2	(3.1 ± 0.2) × 10^{17}
I17158−3901c2^S	17:19:20.47	−39:03:49.20	2.8	152 ± 3	(1.5 ± 0.1) × 10^{15}	(1.4 ± 0.1) × 10^{-3}				150	1.1 × 10^{17}
I17175−3544^E	17:20:53.42	−35:46:57.72	3.4	174 ± 9	(5.4 ± 0.2) × 10^{16}	(8.6 ± 0.4) × 10^{-3}	183 ± 8	(1.4 ± 0.1) × 10^{18}	(2.2 ± 0.1) × 10^{-1}	182 ± 6	(6.3 ± 0.1) × 10^{18}
I17220−3609^{E,S}	17:25:25.22	−36:12:45.34	1.6	183 ± 14	(1.6 ± 0.1) × 10^{16}	(5.7 ± 0.3) × 10^{-3}	173 ± 22	(3.8 ± 0.1) × 10^{17}	(1.4 ± 0.1) × 10^{-1}	176 ± 6	(2.8 ± 0.1) × 10^{18}
I17233−3606^{E,S}	17:26:42.46	−36:09:17.85	3.9	160 ± 4	(3.9 ± 0.1) × 10^{16}	(4.1 ± 0.2) × 10^{-2}	100 ± 14	(8.9 ± 0.5) × 10^{16}	(9.3 ± 0.6) × 10^{-2}	165 ± 8	(9.6 ± 0.4) × 10^{17}
I17441−2822^E	17:47:20.17	−28:23:04.74	1.3	160 ± 18	(2.5 ± 0.1) × 10^{16}	(1.8 ± 0.1) × 10^{-2}	144 ± 7	(9.6 ± 0.2) × 10^{16}	(6.9 ± 0.2) × 10^{-2}	207 ± 8	(1.4 ± 0.1) × 10^{18}
I18032−2032c1	18:06:14.92	−20:31:43.22	0.9				204 ± 17	(1.2 ± 0.1) × 10^{17}	(1.1 ± 0.1) × 10^{-1}	204	1.1 × 10^{18}
I18032−2032c2	18:06:14.88	−20:31:39.59	2.4	127 ± 5	(2 ± 0.1) × 10^{16}	(4 ± 0.3) × 10^{-2}	130 ± 12	(7 ± 0.2) × 10^{16}	(1.5 ± 0.4) × 10^{-1}	146 ± 5	(4.7 ± 0.2) × 10^{17}
I18032−2032c3	18:06:14.80	−20:31:37.26	1.1	110 ± 3	(2.4 ± 0.1) × 10^{15}	(4 ± 0.3) × 10^{-2}				110	1.8 × 10^{17}
I18032−2032c4	18:06:14.66	−20:31:31.57	2.1	130 ± 16	(8 ± 0.1) × 10^{15}	(3.8 ± 0.1) × 10^{-3}	140 ± 13	(1.7 ± 0.2) × 10^{17}	(8.1 ± 0.3) × 10^{-2}	157 ± 8	(2.1 ± 0.1) × 10^{18}
I18056−1952^S	18:08:38.23	−19:51:50.31	1.1	285 ± 9	(1.9 ± 0.1) × 10^{18}	(6.3 ± 0.1) × 10^{-2}	133 ± 5	(2.1 ± 0.1) × 10^{18}	(7 ± 0.3) × 10^{-2}	226 ± 9	(3 ± 0.1) × 10^{19}

Table 1 – *continued*

Source	RA	Dec.	θ_{source}		C_2H_5CN			CH_3OCHO		CH_3OH	
	(^{h} ^{m} ^{s})	($^\circ$ $'$ $''$)	(arcsec)	T_{rot} (K)	N (cm^{-2})	f	T_{rot} (K)	N (cm^{-2})	f	T_{rot} (K)	N (cm^{-2})
I18089−1732	18:11:51.45	−17:31:28.96	1.7	277 ± 9	$(4.1 \pm 0.1) \times 10^{16}$	$(1.6 \pm 0.1) \times 10^{-2}$	128 ± 14	$(2.3 \pm 0.5) \times 10^{17}$	$(8.8 \pm 0.2) \times 10^{-2}$	200 ± 7	$(2.6 \pm 0.1) \times 10^{18}$
I18117−1753^S	18:14:39.51	−17:52:00.08	1.6	180 ± 28	$(9.5 \pm 0.1) \times 10^{15}$	$(5.9 \pm 0.2) \times 10^{-3}$	160 ± 25	$(1.3 \pm 0.2) \times 10^{17}$	$(8.1 \pm 1.1) \times 10^{-2}$	163 ± 5	$(1.6 \pm 0.1) \times 10^{18}$
I18159−1648c1	18:18:54.66	−16:47:50.28	1.7	157 ± 26	$(7.6 \pm 0.2) \times 10^{15}$	$(7.6 \pm 0.1) \times 10^{-3}$	161 ± 18	$(2.4 \pm 0.1) \times 10^{17}$	$(2.4 \pm 0.4) \times 10^{-1}$	228 ± 12	$(1.1 \pm 0.2) \times 10^{18}$
I18159−1648c2	18:18:54.34	−16:47:49.97	1.9	104 ± 20	$(1.1 \pm 0.2) \times 10^{15}$	$(1.8 \pm 0.3) \times 10^{-3}$	110 ± 22	$(2.9 \pm 0.3) \times 10^{16}$	$(4.8 \pm 0.4) \times 10^{-2}$	165 ± 11	$(6 \pm 0.1) \times 10^{17}$
I18182−1433^S	18:21:09.05	−14:31:47.88	2.1	120 ± 10	$(1.1 \pm 0.1) \times 10^{15}$	$(5.2 \pm 0.5) \times 10^{-3}$	122 ± 4	$(2.4 \pm 0.2) \times 10^{16}$	$(1.1 \pm 0.1) \times 10^{-1}$	120	2.1×10^{17}
I18236−1205^S	18:26:25.79	−12:03:53.08	1.4	110 ± 8	$(1.8 \pm 0.1) \times 10^{15}$	$(1.1 \pm 0.1) \times 10^{-2}$				138 ± 20	$(1.7 \pm 0.1) \times 10^{17}$
I18290−0924^S	18:31:44.13	−09:22:12.25	1.4	120 ± 4	$(3.3 \pm 0.9) \times 10^{15}$	$(5.8 \pm 1.6) \times 10^{-3}$				120	5.7×10^{17}
I18316−0602	18:34:20.91	−05:59:42.0	2.9	186 ± 35	$(2.8 \pm 0.1) \times 10^{15}$	$(3.2 \pm 0.1) \times 10^{-3}$	108 ± 204	$(2.1 \pm 0.15) \times 10^{16}$	$(2.4 \pm 0.2) \times 10^{-2}$	167 ± 7	$(8.7 \pm 0.3) \times 10^{17}$
I18411−0338^S	18:43:46.23	−03:35:29.77	1	134 ± 4	$(9.6 \pm 0.5) \times 10^{15}$	$(1.1 \pm 0.1) \times 10^{-2}$	160 ± 15	$(7 \pm 0.1) \times 10^{16}$	$(7.7 \pm 0.5) \times 10^{-2}$	160 ± 14	$(9.1 \pm 0.6) \times 10^{17}$
I18469−0132$^{E,\,S}$	18:49:33.05	−01:29:03.34	0.9	124 ± 8	$(5.1 \pm 0.1) \times 10^{15}$	$(3.6 \pm 0.2) \times 10^{-2}$	136 ± 15	$(9.4 \pm 0.2) \times 10^{16}$	$(6.7 \pm 0.4) \times 10^{-2}$	145 ± 9	$(1.4 \pm 0.1) \times 10^{18}$
I18507+0110$^{E,\,S}$	18:53:18.56	+ 01:14:58.23	1.3	172 ± 6	$(9 \pm 0.2) \times 10^{16}$	$(8.2 \pm 0.2) \times 10^{-3}$	200 ± 11	$(1.6 \pm 0.2) \times 10^{18}$	$(1.5 \pm 0.2) \times 10^{-1}$	240 ± 16	$(1.1 \pm 0.1) \times 10^{19}$
I18507+0121	18:53:18.01	+ 01:25:25.56	1.7	160 ± 4	$(3.7 \pm 0.1) \times 10^{16}$	$(8.8 \pm 0.3) \times 10^{-3}$	200 ± 12	$(6.1 \pm 0.1) \times 10^{17}$	$(1.5 \pm 0.1) \times 10^{-1}$	220 ± 8	$(4.2 \pm 0.1) \times 10^{18}$
I18517+0437^S	18:54:14.24	+ 04:41:40.65	2.3	190 ± 30	$(8 \pm 1) \times 10^{14}$	$(8.4 \pm 1.1) \times 10^{-4}$	140 ± 23	$(2.8 \pm 0.3) \times 10^{16}$	$(2.9 \pm 0.4) \times 10^{-2}$	164 ± 8	$(9.5 \pm 0.3) \times 10^{17}$
I19078+0901c1$^{E,\,S}$	19:10:13.16	+ 09:06:12.49	1.7	140 ± 22	$(2.5 \pm 0.2) \times 10^{15}$	$(1.5 \pm 0.1) \times 10^{-2}$				140	1.7×10^{17}
I19078+0901c2	19:10:14.13	+ 09:06:24.67	1.8	120 ± 12	$(3.2 \pm 0.2) \times 10^{15}$	$(1.5 \pm 0.1) \times 10^{-2}$	115 ± 6	$(4.6 \pm 0.3) \times 10^{16}$		170 ± 8	$(8.7 \pm 0.3) \times 10^{17}$
I19095+0930$^{E,\,S}$	19:11:53.99	+ 09:35:50.27	0.5	160 ± 11	$(7.5 \pm 0.2) \times 10^{15}$	$(1.8 \pm 0.1) \times 10^{-3}$	121 ± 3	$(1.3 \pm 0.1) \times 10^{17}$	$(3.1 \pm 0.1) \times 10^{-2}$	156 ± 15	$(4.2 \pm 0.1) \times 10^{18}$

Note. The superscript E in column 1 indicates that the hot core is externally heated, while S denotes that there is spatial separation between nitrogen- and oxygen-bearing molecules. θ_{source} is the source size derived from the deconvolved continuum size on assuming $\pi\theta^2 = \pi ab$, where a and b are the major and minor axes of the continuum source from Gaussian fitting. f denotes the relative abundance of the molecular species (C_2H_5CN or CH_3OCHO) with respect to CH_3OH.

for eXternal numerical codes (MAGIX; Möller et al. 2013) for further calculation. Note that we only consider line-rich species of C_2H_5CN, CH_3OCHO, and CH_3OH molecules in this work.

The frequency setup covers many of C_2H_5CN and CH_3OCHO transitions in SPWs 7 and 8. The observed C_2H_5CN and CH_3OCHO transitions span upper level energies of 30–139 and 22–58 K, respectively. Therefore, we do not expect very hot gas components to be detected. Only a few CH_3OH lines are tuned in our observations with upper level energies ranging from 17 to 724 K. More than three transitions of C_2H_5CN and CH_3OCHO are detected in the 59 line-rich cores. The line transitions of C_2H_5CN and CH_3OCHO in IRAS 09018−816 are too weak to derive the rotation temperature, but three CH_3OH transitions are detected. Rotation temperatures and column densities can be derived simultaneously. The XCLASS calculations suggested that all the 59 line-rich cores have gas temperatures higher than 100 K, derived from C_2H_5CN and CH_3OCHO. IRAS 09018−4816 has a gas temperature above 100 K based on CH3OH line data. Considering the distances (Liu et al. 2021a) and source sizes, the 60 cores have source sizes smaller than 0.1 pc. We then confirm the 60 cores as hot cores, and give their coordinates, rotation temperatures, and column densities in Table 1. We have checked the literature and found that 15 of these hot cores have been reported before (I18089−1732, Beuther et al. 2004; I16060−5146, I16065−5158, I12326−6245, I14498−5856, and I15254−5621, Araya et al. 2005; Mookerjea et al. 2007; I18507+0110/G34.43+0.24, Beltrán et al. 2009; Dedes et al. 2011; IRAS 18056−1952/G10.47+0.03, Rolffs et al. 2011; I18507+0121/G34.26+0.15, Sakai et al. 2013; Calcutt et al. 2014; I16547−4247, I17233−3606, and I18182−1433, Hernández-Hernández et al. 2014; I18032−2032/G9.62+0.19, Liu et al. 2015; I17175−3544/NGC 6334I, Brogan et al. 2016; Fu & Lin 2016; I17441−2822/Sgr B2(M), Sánchez-Monge et al. 2017; Dall'Olio et al. 2019). Thus, 45 hot cores are newly detected in our work. This is currently the largest hot core sample observed with similar angular resolution and spectral coverage. 41 cores have more than three CH_3OH transitions detected. Note that this is a lower limit since the frequency setup of C43-2 and C43-3 configurations has a 48 MHz difference, which leads to two CH_3OH transitions not covered in C43-3 observations. For CH_3OH with less than three transitions detected, column densities are estimated by assuming gas temperatures equal to the rotation temperatures of the oxygen-bearing molecule CH_3OCHO, or equal to the rotation temperatures of C_2H_5CN in case that CH_3OCHO is not detected.

Fig. 1 presents sample spectra towards a few hot cores with modelled molecular spectra (C_2H_5CN, CH_3OCHO, and CH_3OH) overlaid on the observed ones. Clearly, lots of C_2H_5CN and CH_3OCHO lines are observed, and a large number of lines are emitted from C_2H_5CN and CH_3OCHO species. The spectra emitted from the hot cores also show different emission features. From Fig. 1 and the figures in the Supporting Information available online, one can see that line peak intensities of C_2H_5CN are larger than those of CH_3OCHO in 19 cores, while the opposite is seen in 5 cores. It is worth mentioning that C_2H_5CN line emission is absent in four cores, while CH_3OCHO is not detected in nine cores. The differences in line emissions from these cores may imply differences in physical and chemical environments among these sources.

3.2 Line images

Line images of various molecules can provide valuable information on their spatial distributions and possible chemical routes. We choose three molecular line transitions of C_2H_5CN, CH_3OCHO, and CH_3OH at 98 523, 98 792, and 100 639 MHz for the images, respectively. The sample images are shown in Fig. 2, and other images are presented in the Supporting Information available online. Overall, most of the C_2H_5CN, CH_3OCHO, and CH_3OH emissions are associated with the continuum images, though there are position offsets between peaks of the line and continuum images. All the line images show compact source structure and the three line emissions mainly distribute over small regions, indicating hot core properties. It can be seen that the emission peaks of C_2H_5CN are coincident with those of CH_3OCHO in 28 cores. Considering a position accuracy of 0.3 arcsec in line images, 29 cores clearly show nitrogen and oxygen separation, i.e. the emissions of C_2H_5CN and CH_3OCHO peak at different positions. So far, only a few hot cores exhibit nitrogen and oxygen differentiation in space. Our observations provide the largest hot core sample with positional separation between nitrogen- and oxygen-bearing molecules.

3.3 Rotation temperatures, column densities, and abundances relative to CH_3OH

From Table 1, one can see that the rotation temperatures of C_2H_5CN, CH_3OCHO, and CH_3OH are in the ranges 100–285, 100–230, and 100–290 K, respectively. Most of the cores have gas temperatures of 100–200 K for the three species. When compared with C_2H_5CN and CH_3OCHO, CH_3OH has the largest column densities ranging from 8.6×10^{16} to 1.5×10^{19} cm^{-2}, which is two to three orders of magnitude higher than those of C_2H_5CN and one to two orders of magnitude higher than those of CH_3OCHO. Fig. 3 shows the relationships between rotation temperatures and column densities for the three molecules in our sample. Column densities of CH_3OH increase as their rotation temperatures rise. A linear fitting to the data gives $\log(N(CH_3OH)) = 0.022T_{\rm rot} + 14$ with a correlation coefficient of 0.86. A similar trend is seen for CH_3OCHO with the relation $\log(N(CH_3OCHO)) = 0.017T_{\rm rot} + 14$ and a correlation coefficient of 0.68. The linear fitting to C_2H_5CN data gives a correlation coefficient of 0.29, suggesting that column densities of C_2H_5CN are not sensitive to its rotation temperatures, though a weak increasing trend is seen. The results appear to indicate that the two oxygen-bearing molecules are chemically related species or the two species reside in the same astrophysical environments.

Fig. 4 presents the relationships of column densities among the three species. Overall, column densities of both C_2H_5CN and CH_3OCHO have a positive correlation with that of CH_3OH. The linear fittings give $\log(N(CH_3OCHO)) = 1.1\log(N(CH_3OH))–2.5$ and $\log(N(C_2H_5CN)) = 1.2\log(N(CH_3OH))–5.1$ with correlation coefficients of 0.95 and 0.82 for CH_3OCHO and C_2H_5CN, respectively. The models suggested that the oxygen-bearing molecules CH_3OCHO and CH_3OH and the nitrogen-bearing molecule C_2H_5CN have different forming pathways (Charnley, Tielens & Millar 1992; Rodgers & Charnley 2001). Probably, the column densities of the three molecules depend on the initial cloud environments. As shown in Fig. 3, the column densities of the oxygen-bearing molecules CH_3OCHO and CH_3OH correlate well with the rotation temperatures, while the nitrogen-bearing molecule C_2H_5CN does not follow the same trend. A possible explanation is that excitation of CH_3OCHO and CH_3OH depends on both temperature and density, while excitation of C_2H_5CN is mainly related to its column density.

Among the detected COMs so far, CH_3OH has the highest gas-phase abundance relative to H_2. The infrared observations have shown that CH_3OH is the most abundant molecule relevant to water ice (e.g. Dartois et al. 1999; Ehrenfreund & Charnley 2000; Gibb et al. 2000b). Grain-surface chemical models also suggested that

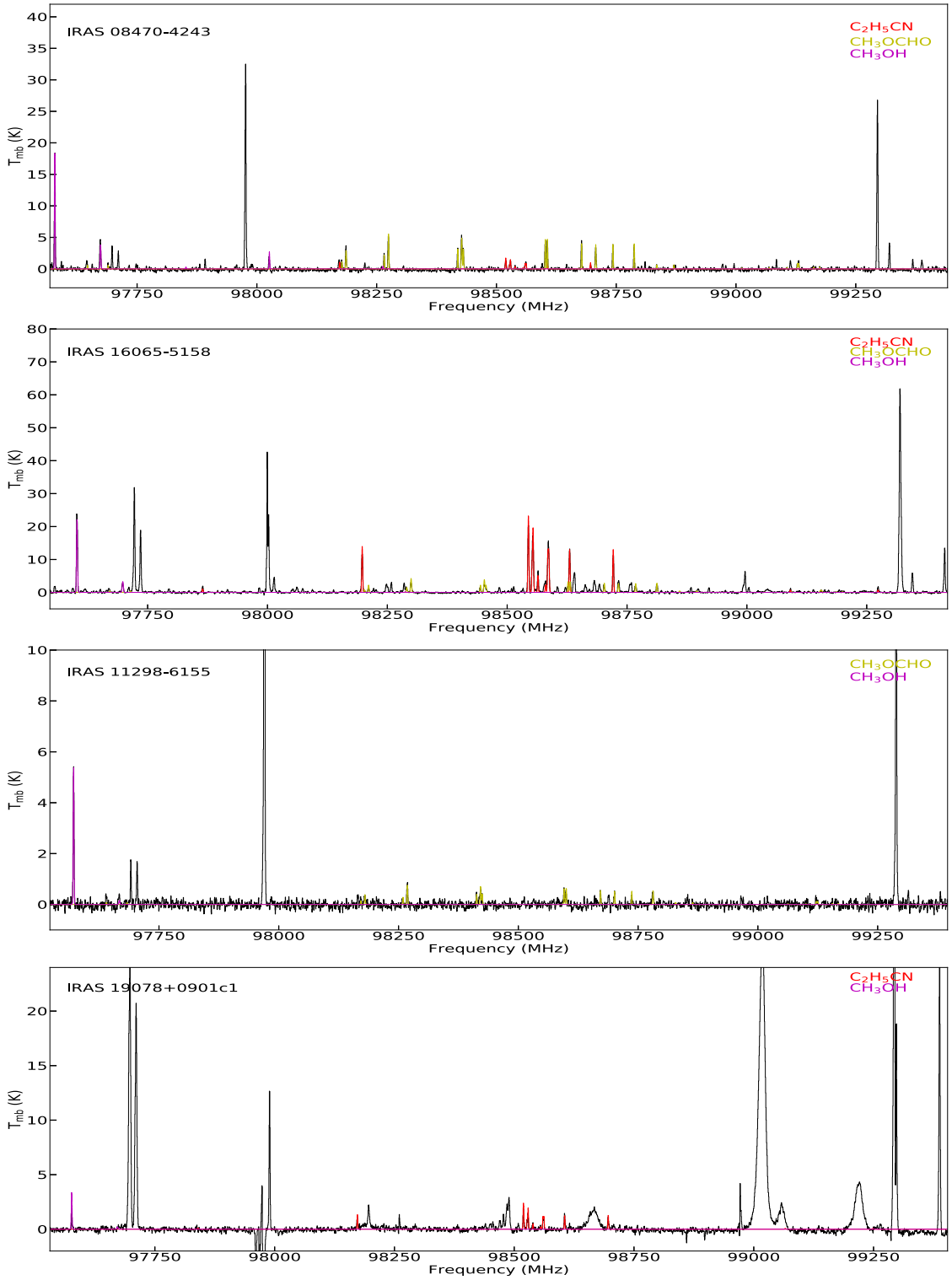

Figure 1. Sample spectra in SPW 7 for four typical hot cores. The observed spectra are shown as black curves and the XCLASS modelled spectra are coded in colour. The spectra of the other sources are available in the supplementary material.

the formation of many of other COMs (especially the oxygen-bearing molecules) is related to CH_3OH. From the abundance criteria, the CH_3OH can be taken as one of the reference molecules to compare with other sources. The relative abundances defined by $f = N(x)/N(CH_3OH)$ are listed in Table 1, where x is the specific molecule CH_3OCHO or C_2H_5CN. The relative abundances range from 8.4×10^{-4} to 4×10^{-2} for C_2H_5CN and from 2.2×10^{-2} to 2.8×10^{-1} for CH_3OCHO, respectively, which are in agreement with previous results in hot cores (Mookerjea et al. 2007; Qin et al. 2010; Feng et al. 2016; Allen et al. 2017; Bonfand et al. 2017, 2019; Guzmán et al. 2018; Bøgelund et al. 2019; Molet et al. 2019; Law et al. 2021).

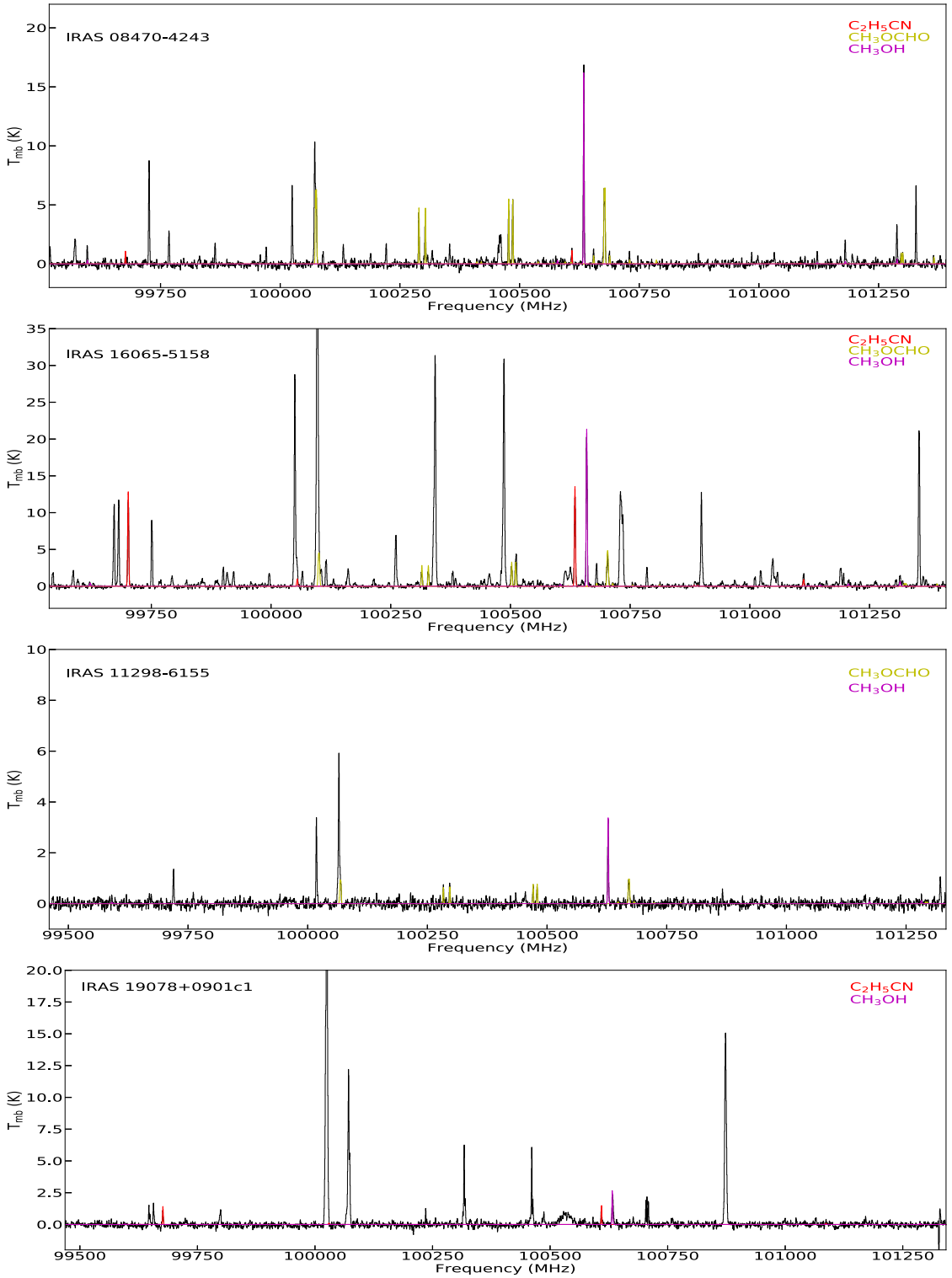

Figure 1. *continued* Sample spectra in SPW 8 for four typical hot cores. The observed spectra are shown as black curves and the XCLASS modelled spectra are coded in colour. The spectra of all the sources are available in the supplementary material.

4 DISCUSSION

4.1 Heating mechanism

Observationally, the evolutionary sequence of high-mass star formation starts from massive pre-stellar cores to high-mass protostellar objects (HMPOs), hot cores, hypercompact H II (HC H II) and UC H II regions, where massive stars are already formed (e.g. Menten, Pillai & Wirowski 2005; Beuther et al. 2007). During the processes of massive star formation, the gravitational energy is converted into thermal energy to form the HMPOs. The radiation from HMPOs, HC

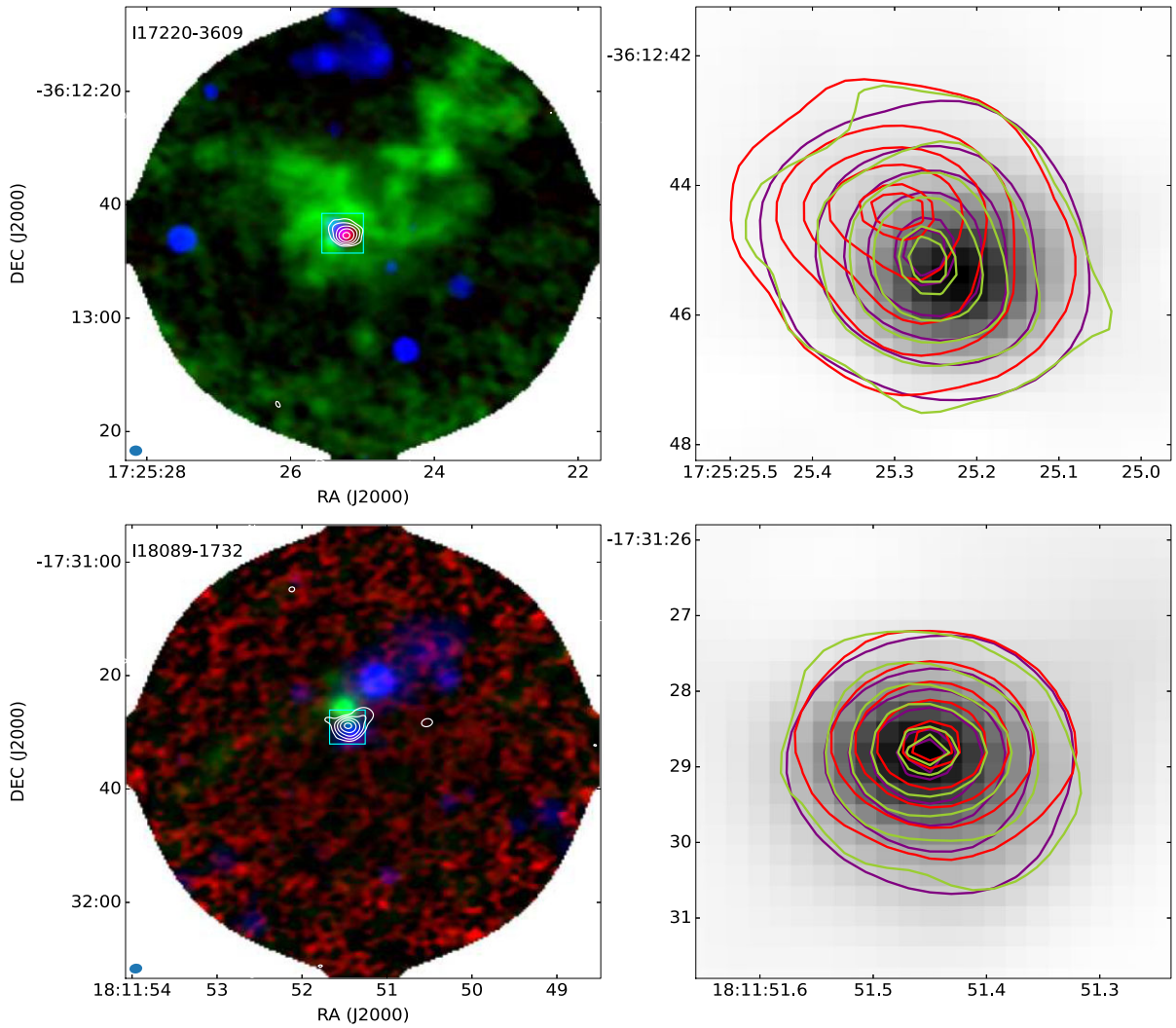

Figure 2. Sample images of the continuum and organic molecular lines. In the left-hand panels, the background shows the three-colour image composed of H40α (red), SiO (green), and *Spitzer* 4.5 μm (blue), and the white contours represent the 3 mm continuum; the green rectangles mark the imaging regions of the right-hand panels. In the right-hand panels, the background shows the 3 mm continuum. The red, cyan, and yellow contours represent the integrated intensities of C_2H_5CN, CH_3OH, and CH_3OCHO, respectively. The contour levels are 10 to 90 per cent (stepped by 20 per cent) of the peak values. The innermost contour has a level of 95 per cent of the peak value. The images of all the sources are available in the supplementary material.

H II and UC H II regions can heat up their immediate environments to form hot cores. Therefore, hot cores are observed to be associated with dense and hot regions near the young HMPOs and the UC H II regions.

In this section, we want to differentiate internal and external heating mechanisms by comparing the relative position of line images of COMs and UC H II regions. Radio continuum at centimetre wavelength and radio recombination lines are characteristics of the UC H II regions associated with newly formed high-mass young stars. ATOMS covers the H40α line transition, which can be used for identifying UC H II regions. Fig. 2 presents sample images of the continuum, organic molecular, H40α, and SiO lines. From the left-hand panels of Fig. 2 and the figures in the Supporting Information available online, 28 UC H II regions are identified based on H40α line images. When comparing the continuum and H40α images with the CH_3OH line images, we find that the morphologies of CH_3OH line images are similar to those of continuum images, and that the CH_3OH emissions peak at the peak positions of the continuum, for most sources without associated UC H II regions. We note that although IRAS 08303−4303, IRAS 13484−6100, IRAS 16484−4603, IRAS 17158−3901, IRAS 17233−3606, and IRAS 18182−1433 have no UC H II region counterparts, their CH_3OH emission peaks are located offset from those of continuum emissions. Probably, shocks traced by the 4.5 μm and SiO push the molecular materials away. For the sources having H40α line emission, peaks of CH_3OH are offset from the continuum images except for IRAS 18056−1952. Previous molecular line images were observed to be not always consistent with the continuum emission in the cases where continuum emission includes contributions from dust and free–free emission of UC H II regions. Also no internal energy sources were identified, suggesting that these hot cores are externally heated (e.g. Wyrowski et al. 1999; De Buizer et al. 2003; Mookerjea et al. 2007). Then we simply classify the observed hot cores in our work into two categories: externally heated hot cores and internally heated hot cores. 24 hot cores are thought to be heated by adjacent UC H II regions, and the other sources are classified as internally heated hot cores, suggesting

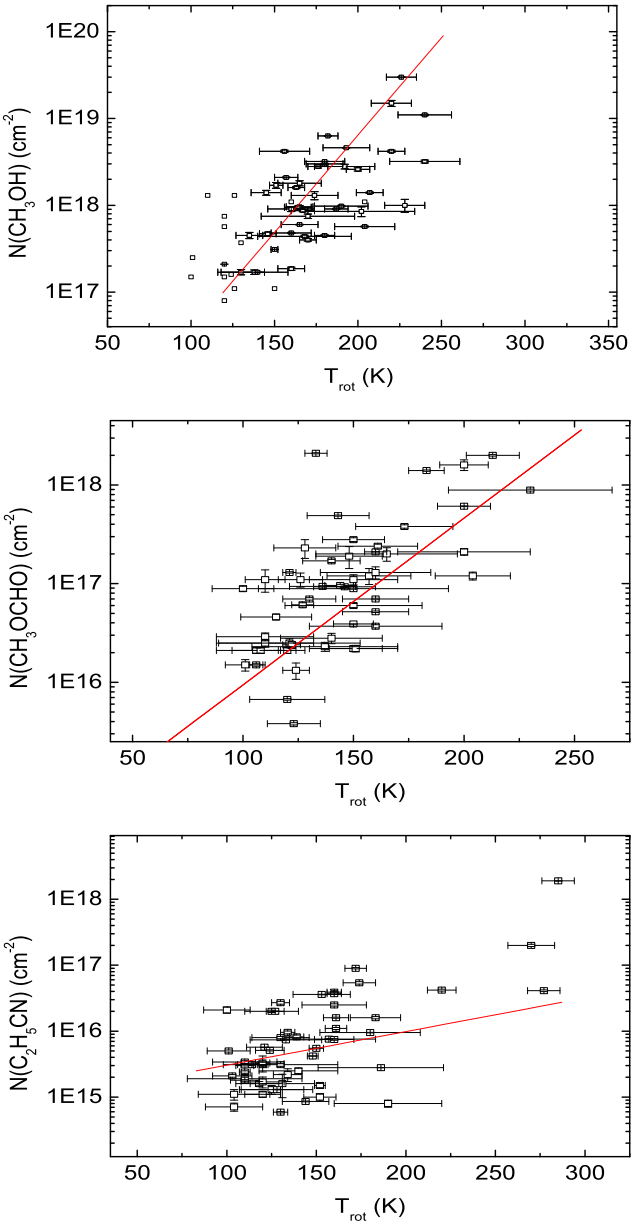

Figure 3. Relationships between column densities and rotation temperatures for CH_3OH, CH_3OCHO, and C_2H_5CN. The open squares indicate the derived column densities and rotation temperatures for the hot cores. The bars indicate the 1σ errors. The data points without error bars in the upper panel are for the sources without three CH_3OH lines detected. The linear least-squares fit is shown as a red solid line.

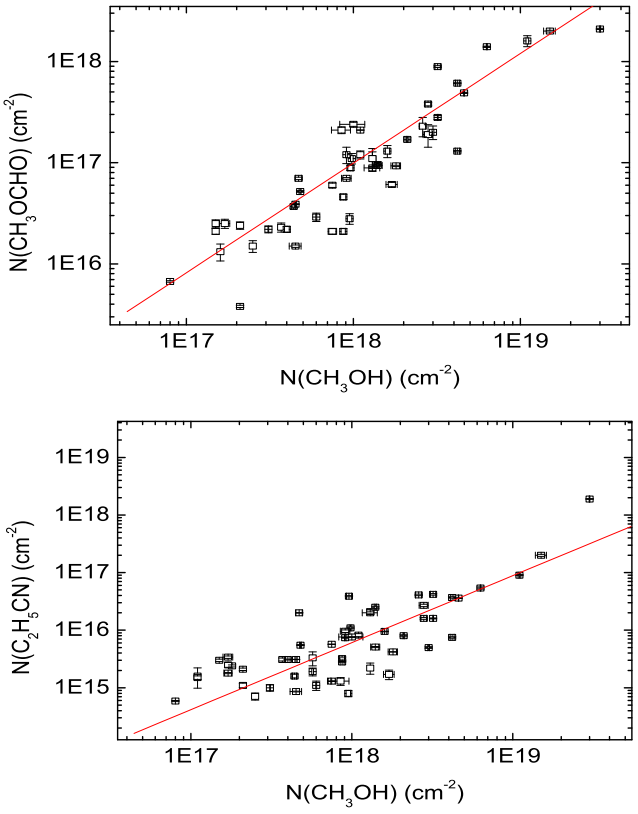

Figure 4. Correlations of column densities of CH_3OH, CH_3OCHO, and C_2H_5CN. The open squares indicate the column densities and the bars indicate the 1σ errors. The linear least-squares fit is shown as a red solid line.

that some hot cores are not simply linked to HMPOs and precursors to UC H II regions in the evolutionary sequence during massive star formation (Law et al. 2021), but they only trace physical and chemical environments of hot, dense, and line-rich regions. Note that we consider IRAS 18056−1952 and I18032−2032c1 as internally heated since both line and continuum images of the two sources peak at UC H II region positions.

Fig. 5 shows the cumulative distributions of the rotational temperatures and column densities of C_2H_5CN and CH_3OCHO of the two groups of hot cores, the internally heated ones and the externally heated ones, respectively. No statistical difference of the rotational temperatures of C_2H_5CN between the two groups can be found. The rotational temperatures of CH_3OCHO tend to be higher in the externally heated hot cores than in the internally heated hot cores, although this difference is not very much significant with a p-value of 0.14 given by the Kolmogorov–Smirnov (KS) test. The externally and internally heated cores show no obvious difference (with a p-value of 0.25) in the cumulative distributions of the column densities of CH_3OCHO. While significant difference (with a p-value of 0.027) can be seen between the cumulative distributions of the column densities of C_2H_5CN ($N_{C_2H_5CN}$), the values of $N_{C_2H_5CN}$ in the externally heated hot cores are a factor of 2 higher than those in the internally heated hot cores. Of course, one may expect that higher temperature components from highly excited lines are shifting towards the UC H II regions for the externally heated hot cores, while higher temperature components will be located at the dusty continuum peaks for internally heated hot cores. Future high-angular-resolution and high-frequency observations covering high-energy line transitions can verify the occurrence and characteristics of externally and internally heated mechanisms in detail.

4.2 Nitrogen and oxygen differentiation

Nitrogen and oxygen differentiation has been suggested in some hot cores (Blake et al. 1987; Wyrowski et al. 1999; Qin et al. 2010, 2015; Fayolle et al. 2015), showing different rotation temperatures and abundances, and nitrogen- and oxygen-bearing COMs peaking at different spatial positions. Observations have shown that many hot cores have excitation temperatures of nitrogen-bearing COMs higher than those of oxygen-bearing COMs (van 't Hoff et al. 2020, and references therein). Derived abundances of oxygen- and nitrogen-

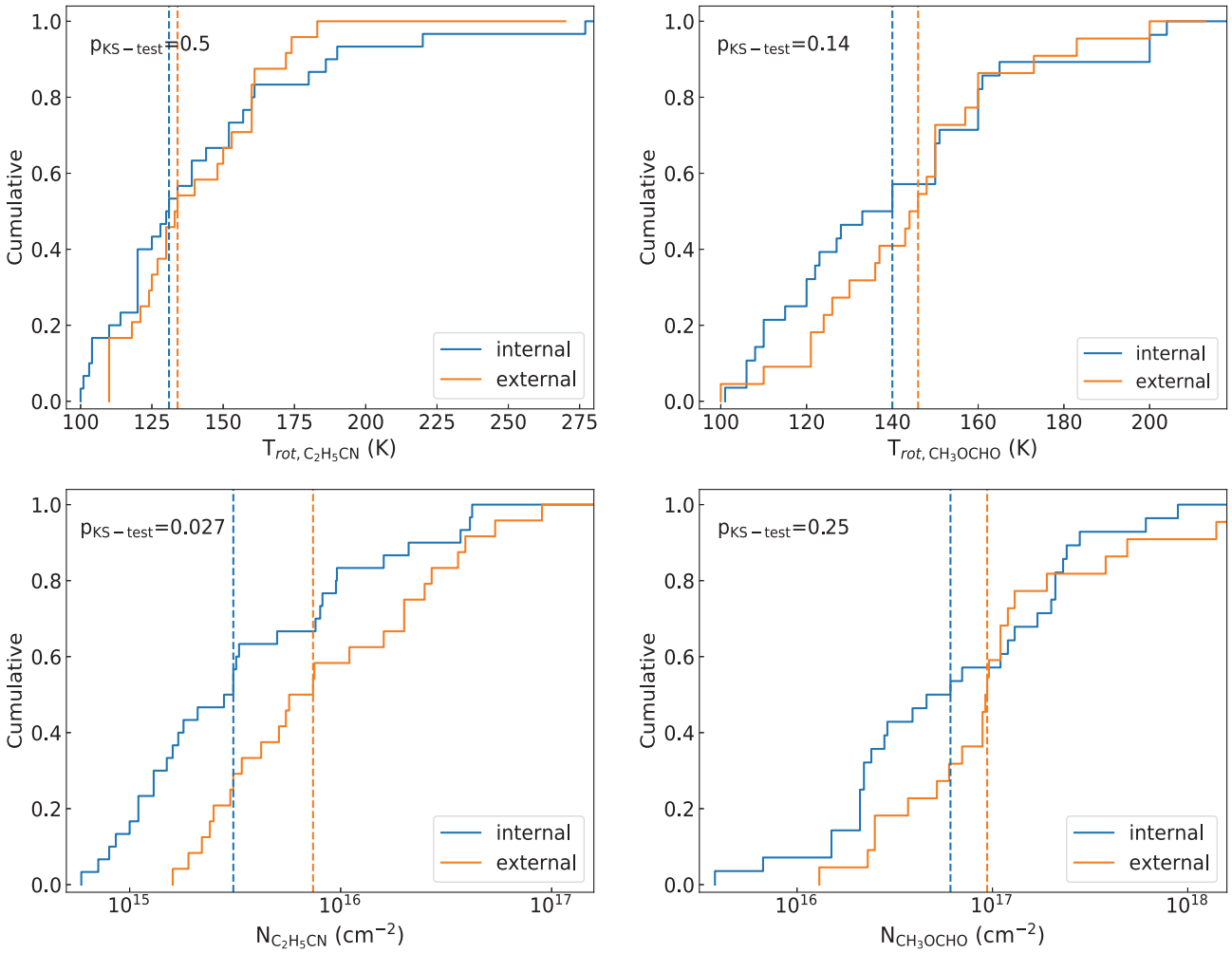

Figure 5. The cumulative distributions of the rotational temperatures (upper panels) and column densities (lower panels) of C_2H_5CN (left-hand panels) and CH_3OCHO (right-hand panels). The parameters of the internally heated ones and the externally heated ones are shown in blue and orange colours, respectively. The vertical dashed lines represent the corresponding median values. The *p*-value of the KS test between the cumulative distributions of the two groups of hot cores is shown in the upper left-hand corner of each panel.

bearing COMs have positive correlations with the other oxygen- and nitrogen-bearing COMs, respectively (e.g. Bisschop et al. 2007; Bergner et al. 2017; Suzuki et al. 2018). The observations have also shown that nitrogen-bearing COMs peak at a protostar position, while oxygen-bearing COMs are peaked offset from the central source (Qin et al. 2010; Fayolle et al. 2015).

From Table 1, rotation temperatures of C_2H_5CN in most hot cores are generally lower than those of CH_3OH, which is inconsistent with previous observations. As stated in Section 3.1, a possible explanation is that our 3 mm observations of C_2H_5CN lines have low upper level energies of 30–139 K, and then the hot components of the cores are not sampled. The LTE calculations find CH_3OCHO and CH_3OH molecules to have larger column densities than that of the nitrogen-bearing molecule C_2H_5CN. The column density of CH_3OH correlates well with that of CH_3OCHO, but also has a positive correlation with C_2H_5CN, which also conflicts with previous results as stated above. Probably, our targeted lines of the C_2H_5CN and CH_3OCHO have low upper level energies, which only sample the freshly evaporated species, and then cannot probe the innermost and hottest structure of the hot cores. Nitrogen and oxygen separation is clearly seen in 29 hot cores, in which C_2H_5CN and oxygen-bearing molecules peak at different spatial positions (see Fig. 2 and the figures in the Supporting Information available online).

4.3 Chemistry

COMs are suggested to be particularly important in both astrophysics and astrochemistry, but also to be linked to the origin of life. However, no firm conclusions about their formation are reached, even for commonly detected CH_3OCHO and C_2H_5CN. Various chemical models are proposed to interpret their origination (Millar, Herbst & Charnley 1991; Charnley et al. 1992, 1995; Caselli, Hasegawa & Herbst 1993; Rodgers & Charnley 2001, 2003; Garrod & Herbst 2006; Garrod, Widicus Weaver & Herbst 2008; Öberg et al. 2009; Taquet, Ceccarelli & Kahane 2012; Choudhury et al. 2015; Taquet et al. 2015; Taquet, Wirström & Charnley 2016; Pols et al. 2018). In summary, main chemical routes are gas-phase and grain-surface chemical reactions as well as interaction between gas-phase and grain-surface molecules. Large sample observations of their relative abundances and spatial distributions will be able to provide clues in investigating their forming pathways.

Higher gas-phase abundances of CH_3OH are derived from (sub)millimetre-wavelength observations towards massive star formation regions, which is attributed to icy CH_3OH evaporated from grain mantles, leading to a large abundance by various chemical models. From Fig. 3, column densities of CH_3OH increase as rotation temperatures rise, providing additional evidence that CH_3OH originates from the grain surface and is then released into gas phase when the gas temperature is higher than 100 K. Our large sample observations give a positive correlation between CH_3OH and CH_3OCHO, which appears to indicate that CH_3OCHO is formed in gas phase and is related to the evaporated CH_3OH as proposed by Charnley et al. (1992, 1995). However, gas-phase mechanisms by molecule–ion reactions have very low efficiency in producing CH_3OCHO (Horn et al. 2004; Geppert et al. 2005). The relationship between the observed column densities and rotation temperatures of CH_3OCHO shows the same trend as of CH_3OH, which has also been reported by previous observations (Law et al. 2021), which may hint that CH_3OCHO also originates from the grain surface and then is evaporated into phase as temperature increases. The warm-up model developed by Garrod et al. (2006) suggested that CH_3OCHO is mainly synthesized on the grain surface at lower temperatures and gas-phase reactions play a dominant role in forming CH_3OCHO when the gas temperature is above 200 K. In this scheme, the formation of CH_3OCHO is attributed to both grain-surface and gas-phase reactions. In our case, the observations of CH_3OCHO transitions at 3 mm band have low upper level energies and should sample freshly evaporated species. The rotation temperatures of CH_3OCHO in most cores are lower than 200 K. We then favour that CH_3OCHO observed by us at a lower frequency band is synthesized on the grain surface. Future higher angular resolution observations of high-energy level lines can detect inner and even hotter components of the hot cores, and can test if the gas-phase reactions play an important role in forming CH_3OCHO.

C_2H_5CN can be formed by ion–molecule reactions in gas phase, but the processes are quite slow. Grain-surface reactions through hydrogenation of HC_3N are a more efficient mechanism (Blake et al. 1987; Caselli et al. 1993; Charnley et al. 2004). Contrary to the two complex oxygen-bearing molecules, the column densities of C_2H_5CN did not show a positive correlation with its rotation temperatures. A possible explanation is that C_2H_5CN tends to have a higher gas temperature than the oxygen-bearing COMs, while our lower energy level lines can only trace lower excitation temperatures in the outer envelopes of the hot cores (Öberg et al. 2013). Large amounts of C_2H_5CN are not fully evaporated from the grain surface. Surprisingly, the column densities of C_2H_5CN correlate well with those of CH_3OH, which is inconsistent with previous observations. Previous observations have shown that nitrogen-bearing molecules have a strong correlation with other nitrogen-bearing molecules and no correlation with oxygen-bearing COMs (Bisschop et al. 2007; Bergner et al. 2017; Suzuki et al. 2018). As argued before, our observations may only sample freshly evaporated species, which have not involved in subsequent gas-phase reactions yet. The observed correlation between C_2H_5CN and CH_3OH may reflect initial chemical environments or physical differences (van 't Hoff et al. 2020).

The spatial separation between C_2H_5CN and the two oxygen-bearing molecules can be seen from Fig. 2 and figures in the Supporting Information available online. But no obvious temperature differentiation is observed as in Orion KL, W3(OH) complex, and G34.26+0.15 (Blake et al. 1987; Wyrowski et al. 1999; Mookerjea et al. 2007; Crockett et al. 2014; Qin et al. 2015), due to our targeted lines having low upper level energies. Another reason is that in most cases our beam may cover part of both nitrogen and nitrogen cores. Nitrogen and oxygen differentiation is a long-standing problem. Different chemical models give different explanations (Caselli et al. 1993; Rodgers & Charnley 2003; Garrod et al. 2008; van 't Hoff et al. 2020). Higher resolution observations of highly excited lines from various COMs towards a large sample of hot cores are needed to interpret the observed differentiation.

5 CONCLUSIONS

We have performed a systematic hot core survey employing C_2H_5CN, CH_3OCHO, and CH_3OH commonly observed in hot cores, based on the data obtained by the ATOMS project. We summarize the main results as follows.

(1) The ATOMS project at 3 mm band was set up to cover multiple C_2H_5CN, CH_3OCHO, and CH_3OH transitions, which were then used for deriving their rotation temperatures and column densities. We identify a dense core as a hot core if more than three transitions of the COMs are identified and have rotation temperatures above 100 K. In total, 60 hot cores are identified, out of which 45 are newly detected, thus representing the largest hot core sample with similar angular resolution and spectral coverage.

(2) The observations have shown that line intensities of C_2H_5CN are stronger than those of CH_3OCHO lines in 19 cores, while the opposite is observed in 5 cores. There is total absence of C_2H_5CN line emission in four cores, while CH_3OCHO lines are not detected in nine cores. Probably, the different spectral features reflect the differences in physical and chemical environments.

(3) Line images of the three molecules show compact source structure concentrated on small regions for the hot cores. There are 28 hot cores associated with UC H II regions. Based on relative positions between UC H II regions and CH_3OH emission peaks, we classify the detected cores into two categories: externally heated and internally heated hot cores. 24 hot cores are externally heated by radiation from adjacent UC H II regions, while the others are heated internally.

(4) Our large sample shows that column densities of CH_3OCHO and CH_3OH correlate well with their rotation temperatures, and column densities of the two molecules have a positive correlation. The results support that CH_3OCHO and CH_3OH originate from the grain-surface chemistry.

(5) Nitrogen and oxygen differentiation is observed in 29 hot cores with nitrogen- and oxygen-bearing molecules peaking at different positions, but no clear differences in temperature and column density are seen from our data.

In summary, our ALMA 12 m array observations provide the largest robust hot core sample with similar angular resolution and spectral coverage. 24 hot cores are considered to be heated by external energy sources, and therefore hot cores may not be considered at the evolutionary sequence of massive star formation. The targeted lines of ATOMS have upper level energies of less than 139 K for C_2H_5CN and CH_3OCHO; hence, the hottest components are not observed. The heating mechanisms as well as nitrogen and oxygen differentiation in rotation temperature is needed to be verified by future observations of highly excited lines of various COMs. The future observations can also test whether gas-phase chemical reactions play an important role in higher temperatures, as suggested by chemical models.

ACKNOWLEDGEMENTS

This work has been supported by the National Key R&D Program of China (No. 2017YFA0402701), by the National Natural Science Foundation of China (grant nos 12033005, 12073061, 12122307, 12103045, 11973013, 11973099, and 11873086), and by the international partnership programme of Chinese Academy of Sciences through grant no. 114231KYSB20200009, Shanghai Pujiang Program 20PJ1415500, and the science research grants from the China Manned Space Project with no. CMS-CSST-2021-B06. This research was carried out in part at the Jet Propulsion Laboratory, which is operated by the California Institute of Technology under contract with NASA. J-EL was supported by the National Research Foundation of Korea (NRF) grant funded by the Korea government (MSIT; grant no. 2021R1A2C1011718). CWL is supported by the Basic Science Research Program through the National Research Foundation of Korea (NRF) funded by the Ministry of Education, Science and Technology (NRF-2019R1A2C1010851). This work is sponsored in part by the Chinese Academy of Sciences (CAS), through a grant to the CAS South America Center for Astronomy (CASSACA) in Santiago, Chile. Chile. G.G. and L.B. acknowledge support by the ANID BASAL project FB210003. SYH acknowledges support from the Ministry of Science and Technology (MoST) with grants 110-2112-M-001-056-. This paper makes use of the following ALMA data: ADS/JAO.ALMA#2019.1.00685.S. ALMA is a partnership of ESO (representing its member states), NSF (USA), and NINS (Japan), together with NRC (Canada), MOST and ASIAA (Taiwan), and KASI (Republic of Korea), in cooperation with the Republic of Chile. The Joint ALMA Observatory is operated by ESO, AUI/NRAO, and NAOJ.

DATA AVAILABILITY

The data underlying this paper are available in the ALMA archive.

REFERENCES

Ahmadi A. et al., 2018, A&A, 618, A46
Allen V., van der Tak F. F. S., Sánchez-Monge Á., Cesaroni R., Beltrán M. T., 2017, A&A, 603, A133
Araya E., Hofner P., Kurtz S., Bronfman L., DeDeo S., 2005, ApJS, 157, 279
Belloche A., Garrod R. T., Müller H. S. P., Menten K. M., Medvedev I., Thomas J., Kisiel Z., 2019, A&A, 628, 10
Belloche A., Müller H. S. P., Garrod R. T., Menten K. M., 2016, A&A, 587, A91
Belloche A., Müller H. S. P., Menten K. M., Schilke P., Comito C., 2013, A&A, 559, A47
Beltrán M. T., Codella C., Viti S., Neri R., Cesaroni R., 2009, ApJ, 690, L93
Bergin E. A. et al., 2010, A&A, 521, L20
Bergner J. B., Öberg K. I., Garrod R. T., Graninger D. M., 2017, ApJ, 841, 120
Beuther H. et al., 2004, ApJ, 616, L19
Beuther H., Churchwell E. B., McKee C. F., Tan J. C., 2007, in Reipurth B., Jewitt D., Keil K., eds, Protostars and Planets V. Univ. Arizona Press, Tucson, p. 165
Beuther H., Zhang Q., Bergin E. A., Sridharan T. K., 2009, AJ, 137, 406
Beuther H., Zhang Q., Sridharan T. K., Chen Y., 2005, ApJ, 628, 800
Bisschop S. E., Fuchs G. W., van Dishoeck E. F., Linnartz H., 2007, A&A, 474, 1061
Blake G. A., Sutton E. C., Masson C. R., Phillips T. G., 1987, ApJ, 315, 621
Bøgelund E. G., Barr A. G., Taquet V., Ligterink N. F. W., Persson M. V., Hogerheijde M. R., van Dishoeck E. F., 2019, A&A, 628, A2
Bonfand M., Belloche A., Garrod R. T., Menten K. M., Willis E., Stéphan G., Müller H. S. P., 2019, A&A, 628, A27
Bonfand M., Belloche A., Menten K. M., Garrod R. T., Müller H. S. P., 2017, A&A, 604, 60
Brogan C. L., Hunter T. R., Cyganowski C. J., Chandler C. J., Friesen R., Indebetouw R., 2016, ApJ, 832, 187
Calcutt H., Viti S., Codella C., Beltrán M. T., Fontani F., Woods P. M., 2014, MNRAS, 443, 3157
Caselli P., Hasegawa T. I., Herbst E., 1993, ApJ, 408, 548
Ceccarelli C. et al., 2017, ApJ, 850, 176
Cesaroni R., 2005, in Cesaroni R., Felli M., Churchwell E., Walmsley M., eds, Proc. IAU Symp. Vol. 227, Massive Star Birth: A Crossroads of Astrophysics. Cambridge Univ. Press, Cambridge, p. 59
Charnley S. B., Ehrenfreund P., Millar T. J., Boogert A. C., Markwick A. J., Butner H. M., Ruiterkamp R., Rodgers S. D., 2004, MNRAS, 347, 157
Charnley S. B., Kress M. E., Tielens A. G. G. M., Millar T. J., 1995, ApJ, 448, 232
Charnley S. B., Tielens A. G. G. M., Millar T. J., 1992, ApJ, 399, L71
Choudhury R., Schilke P., Stéphan G., Bergin E., Möller T., Schmiedeke A., Zernickel A., 2015, A&A, 575, A68
Coletta A., Fontani F., Rivilla V. M., Mininni C., Colzi L., Sánchez-Monge Á., Beltrán M. T., 2020, A&A, 641, A54
Crockett N. R. et al., 2014, ApJ, 787, 112
Csengeri T., Belloche A., Bontemps S., Wyrowski F., Menten K. M., Bouscasse L., 2019, A&A, 632, A57
Dall'Olio D. et al., 2019, A&A, 626, A36
Dartois E., Schutte W., Geballe T. R., Demyk K., Ehrenfreund P., D'Hendecourt L., 1999, A&A, 342, L32
De Buizer J. M., Radomski J. T., Telesco C. M., Pina R. K., 2003, ApJ, 598, 1127
Dedes C., Leurini S., Wyrowski F., Schilke P., Menten K. M., Thorwirth S., Ott J., 2011, A&A, 526, A59
Ehrenfreund P., Charnley S. B., 2000, ARA&A, 38, 427
Fayolle E. C., Öberg K. I., Garrod R. T., van Dishoeck E. F., Bisschop S. E., 2015, A&A, 576, A45
Feng S., Beuther H., Semenov D., Henning Th., Linz H., Mills E. A. C., Teague R., 2016, A&A, 593, A46
Feng S., , Beuther H., Henning Th., Semenov D., Palau A., Mills E. A. C., 2015, A&A, 581, A71
Fontani F., Pascucci I., Caselli P., Wyrowski F., Cesaroni R., Walmsley C. M., 2007, A&A, 470, 639
Fu L., Lin G.-M., 2016, Res. Astron. Astrophys., 16, 182
Fuente A., Treviño-Morales S. P., Alonso-Albi T., Sánchez-Monge A., Rivière-Marichalar P., Navarro-Almaida D., 2021, MNRAS, 507, 1886
Garrod R. T., Herbst E., 2006, A&A, 457, 927
Garrod R. T., Widicus Weaver S. L., Herbst E., 2008, ApJ, 682, 283
Geppert W. D. et al., 2005, JPhCS, 4, 26
Gibb E. et al., 2000b, ApJ, 536, 347
Gibb E., Nummelin A., Irvine W. M., Whittet D. C. B., Bergman P., 2000a, ApJ, 545, 309
Gieser C. et al., 2019, A&A, 631, A142
Gieser C. et al., 2021, A&A, 648, A66
Guzmán A. E., Guzmán V. V., Garay G., Bronfman L., Hechenleitner F., 2018, ApJS, 236, 45
Halfen D. T., Ilyushin V. V., Ziurys L. M., 2013, ApJ, 767, 66
Herbst E., van Dishoeck E. F., 2009, ARA&A, 47, 427
Hernández-Hernández V., Kurtz S., Kalenskii S., Golysheva P., Garay G., Zapata L., Bergman P., 2019, AJ, 158, 18
Hernández-Hernández V., Zapata L. A., Kurtz S., Garay G., 2014, ApJ, 786, 38
Horn A., Møllendal H., Sekiguchi O., Uggerud E., Roberts H., Herbst E., Viggiano A. A., Fridgen T. D., 2004, ApJ, 611, 605
Jiménez-Serra I., Zhang Q., Viti S., Martń-Pintado J., de Wit W. J., 2012, ApJ, 753, 34
Jørgensen J. K., Belloche A., Garrod R. T., 2021, ARA&A, 58, 727
Kalenskii S. V., Johansson L. E. B., 2010, Astron. Rep., 54, 1084
Kurtz S., Cesaroni R., Churchwell E., Hofner P., Walmsley C. M., 2000, in Mannings V., Boss A., Russell S., eds, Protostars and Planets IV. Univ. Arizona Press, Tucson, p. 299

Law C. J., Zhang Q., Öberg K. I., Galván-Madrid R., Keto E., Liu H. B., Ho P. T. P., 2021, ApJ, 909, 214
Lee J.-E. et al., 2019, Nat Astron., 3, 314
Li J. et al., 2020, MNRAS, 492, 556
Ligterink N. F. W., El-Abd S. J., Brogan C. L., Hunter T. R., Remijan A. J., Garrod R. T., McGuire B. M., 2020, ApJ, 901, 37
Liu H.-L. et al., 2021, MNRAS, 505, 2801
Liu S.-Y., Girart J. M., Remijan A., Snyder L. E., 2002, ApJ, 576, 255
Liu S.-Y., Mehringer D. M., Snyder L. E., 2001, ApJ, 552, 654
Liu T. et al., 2015, ApJ, 810, 147
Liu T. et al., 2020a, MNRAS, 696, 2790
Liu T. et al., 2020b, MNRAS, 696, 2821
Luo G., Feng S. Y., Li D., Qin S.-L., Peng Y., Tang N., Ren Z., Shi H., 2019, ApJ, 885, 82
McGuire B. A., 2021, preprint (arXiv:210913848M)
McMullin J. P., Waters B., Schiebel D., Young W., Golap K., 2007, in Shaw R. A., Hill F., Bell D. J., eds, ASP Conf. Ser. Vol. 376, Astronomical Data Analysis Software and Systems XVI. Astron. Soc. Pac., San Francisco, p. 127
Menten K., Pillai T., Wirowski F., 2005, in Cesaroni R., Felli M., Churchwell E., Walmsley M., eds, Proc. IAU Symp. Vol. 227, Massive Star Birth: A Crossroads of Astrophysics. Cambridge Univ. Press, Cambridge, p. 23
Millar T. J., Herbst E., Charnley S. B., 1991, ApJ, 369, 147
Mills E. A. C., Corby J., Clements A. R., Butterfield N., Jones P. A., Cunningham M. R., Ott J., 2018, ApJ, 869, 121
Molet J. et al., 2019, A&A, 626, A132
Möller T., Bernst I., Panoglou D., Muders D., Ossenkopf V., Röllig M., Schilke P., 2013, A&A, 549, A21
Möller T., Endres C., Schilke P., 2017, A&A, 589, A7
Möller T., Schilke P., Schmiedeke A., Bergin E. A., Lis D. C., Sánchez-Monge Á., Schwörer A., Comito C., 2021, A&A, 651, A9
Mookerjea B., Casper E., Mundy L. G., Looney L. W., 2007, ApJ, 659, 447
Mottram J. C. et al., 2020, A&A, 636, A118
Müller H. S. P. et al., 2016, A&A, 587, A92
Müller H. S. P., Schlöder F., Stutzki J., Winnewisser G., 2005, J. Mol. Struct., 742, 215
Müller H. S. P., Thorwirth S., Roth D. A., Winnewisser G., 2001, A&A, 370, L49
Neill J. L. et al., 2014, ApJ, 789, 8
Öberg K. I., Boamah M. D., Fayolle E. C., Garrod R. T., Cyganowski C. J., van der Tak F., 2013, ApJ, 771, 95
Öberg K. I., Garrod R. T., van Dishoeck E. F., Linnartz H., 2009, A&A, 504, 891
Orozco-Aguilera M. T., Zapata L. A., Hirota T., Qin S.-L., Masqué J. M., 2017, ApJ, 847, 66
Ospina-Zamudio J., Lefloch B., Ceccarelli C., Kahane C., Favre C., López-Sepulcre A., Montarges M., 2018, A&A, 618, A145
Pagani L., Favre C., Goldsmith P. F., Bergin E. A., Snell R., Melnick G., 2017, A&A, 604, A32
Palau A. et al., 2017, MNRAS, 467, 2723
Peng Y., Rivilla V. M., Zhang L., Ge J. X., Zhou B., 2019, ApJ, 871, 251
Pickett H. M., Poynter R. L., Cohen E. A., Delitsky M. L., Pearson J. C., Müller H. S. P., 1998, J. Quant. Spectrosc. Radiat. Transfer, 60, 883
Pols S., Schwörer A., Schilke P., Schmiedeke A., Sánchez-Monge Á., Möller Th., 2018, A&A, 614, A123
Qin S.-L., Huang M., Wu Y., Xue R., Chen S., 2008, ApJ, 686, L21
Qin S.-L., Schilke P., Wu J., Wu Y., Liu T., Liu Y., Sánchez-Monge Á., 2015, ApJ, 803, 39
Qin S.-L., Wu Y., Huang M., Zhao G., Li D., Wang J.-J., Chen S., 2010, ApJ, 711, 399
Rathborne J. M., Garay G., Jackson J. M., Longmore S., Zhang Q., Simon R., 2011, ApJ, 741, 120
Reid M. J., Schneps M. H., Moran J. M., Gwinn C. R., Genzel R., Downes D., Roennaeng B., 1988, ApJ, 330, 809
Remijan A., Shiao Y.-S., Friedel D. N., Meier D. S., Snyder L. E., 2004, ApJ, 617, 384
Remijan A., Snyder L. E., Friedel D. N., Liu S.-Y., Shah R. Y., 2003, ApJ, 590, 314
Rivilla V. M., Beltrán M. T., Cesaroni R., Fontani F., Codella C., Zhang Q., 2017, A&A, 598, A59
Rodgers S. D., Charnley S. B., 2001, ApJ, 546, 324
Rodgers S. D., Charnley S. B., 2003, ApJ, 585, 355
Rolffs R., Schilke P., Zhang Q., Zapata L., 2011, A&A, 536, A33
Rong J. et al., 2016, MNRAS, 455, 1428
Sakai T. et al., 2013, ApJ, 775, L31
Sakai T. et al., 2018, ApJ, 857, 35
Sánchez-Monge Á. et al., 2014, A&A, 569, A11
Sánchez-Monge Á. et al., 2017, A&A, 604, A6
Sánchez-Monge Á., Palau A., Estalella R., Kurtz S., Zhang Q., Di Francesco J., Shepherd D., 2010, ApJ, 721, L107
Schilke P., Benford D. J., Hunter T. R., Lis D. C., Phillips T. G., 2001, ApJS, 132, 281
Schilke P., Comito C., Thorwirth S., Wyrowski F., Menten K. M., Güsten R., Bergman P., Nyman L.-Å., 2006, A&A, 454, L41
Schilke P., Groesbeck T. D., Blake G. A., Phillips T. G., 1997, ApJS, 108, 301
Suzuki T., Ohishi M., Hirota T., Saito M., Majumdar L., Wakelam V., 2016, ApJ, 825, 79
Suzuki T., Ohishi M., Saito M., Hirota T., Majumdar L., Wakelam V., 2018, ApJS, 237, 3
Taniguchi K., Guzmán A. E., Majumdar L., Saito M., Tokuda K., 2020, ApJ, 898, 54
Taquet V., Ceccarelli C., Kahane C., 2012, A&A, 538, A42
Taquet V., López-Sepulcre A., Ceccarelli C., Neri R., Kahane C., Charnley S. B., 2015, ApJ, 804, 81
Taquet V., Wirström E. S., Charnley S. B., 2016, ApJ, 821, 46
Tercero B., Cuadrado S., López A., Brouillet N., Despois D., Cernicharo J., 2018, A&A, 620, L6
Tychoniec Ł. et al., 2021, A&A, 655, A65
van 't Hoff M. L. R., Bergin E. A., Jørgensen J. K., Blake G. A., 2020, ApJ, 897, L38
van der Tak F. F. S., van Dishoeck E. F., Caselli P., 2000, A&A, 361, 327
van der Walt S. J., Kristensen L. E., Jørgensen J. K., Calcutt H., Manigand S., el Akel M., Garrod R. T., Qiu K., 2021, A&A, 655, A86
van Dishoeck E. F., Blake G. A., 1998, ARA&A, 36, 317
Widicus Weaver S. L. et al., 2017, ApJS, 232, 3
Wong W.-H., An T., 2018, Res. Astron. Astrophys., 18, 134
Wu Y., Liu T., Qin S.-L., 2014, ApJ, 791, 123
Wyrowski F., Schilke P., Walmsley C. M., Menten K. M., 1999, ApJ, 514, L43
Xie J. et al., 2021, Sci. China Phys. Mech. Astron., 64, 279511
Xue C., Remijan A. J., Burkhardt A. M., Herbst E., 2019, ApJ, 871, 112
Zapata L. A., Schmid-Burgk J., Menten K. M., 2011, A&A, 529, A24
Zinnecker H., Yorke H. W., 2007, ARA&A, 45, 481

SUPPORTING INFORMATION

Supplementary data are available at *MNRAS* online.

Figure 1. Spectra in SPW 7 for the 60 hot cores. The observed spectra are shown as black curves and the XCLASS modelled spectra are coded in colour.

Figure 2. Spectra in SPW 8 for the 60 hot cores. The observed spectra are shown as black curves and the XCLASS modelled spectra are coded in colour.

Figure 3. Images of the continuum and organic molecular lines for externally heated hot cores. In the left-hand panels, the background shows the three-colour image composed of H40α (red), SiO (green), and *Spitzer* 4.5 um (blue), and the white contours represent the 3 mm continuum; the green rectangles mark the imaging regions of the right-hand panels. In the right-hand panels, the background shows the 3 mm continuum. The red, cyan, and yellow contours represent

the integrated intensities of C_2H_5CN, CH_3OH, and CH_3OCHO, respectively. The contour levels are 10 to 90 per cent (stepped by 20 per cent) of the peak values.

Figure 4. Images of the continuum and organic molecular lines for internally heated hot cores. In the left-hand panels, the background shows the three-colour image composed of H40α (red), SiO (green), and *Spitzer* 4.5 um (blue), and the white contours represent the 3 mm continuum; the green rectangles mark the imaging regions of the right-hand panels. In the right-hand panels, the background shows the 3 mm continuum. The red, cyan, and yellow contours represent the integrated intensities of C_2H_5CN, CH_3OH, and CH_3OCHO, respectively. The contour levels are 10 to 90 per cent (stepped by 20 per cent) of the peak values.

Please note: Oxford University Press is not responsible for the content or functionality of any supporting materials supplied by the authors. Any queries (other than missing material) should be directed to the corresponding author for the article.

[1]*Department of Astronomy, Yunnan University, Kunming 650091, People's Republic of China*
[2]*Shanghai Astronomical Observatory, Chinese Academy of Sciences, 80 Nandan Road, Shanghai 200030, People's Republic of China*
[3]*Jet Propulsion Laboratory, California Institute of Technology, 4800 Oak Grove Drive, Pasadena, CA 91109, USA*
[4]*National Astronomical Observatories, Chinese Academy of Sciences, Beijing 100101, People's Republic of China*
[5]*University of Chinese Academy of Sciences, Beijing 100049, People's Republic of China*
[6]*NAOC-UKZN Computational Astrophysics Centre, University of KwaZulu-Natal, Durban 4000, South Africa*
[7]*Center for Astrophysics, Harvard & Smithsonian, 60 Garden Street, Cambridge, MA 02138, USA*
[8]*Department of Astronomy, Peking University, 100871 Beijing, People's Republic of China*
[9]*Departamento de Astronom'ia, Universidad de Chile, Las Condes, 7591245 Santiago, Chile*
[10]*Department of Physics, University of Helsinki, PO Box 64, FI-00014 Helsinki, Finland*
[11]*Korea Astronomy and Space Science Institute, 776 Daedeokdaero, Yuseong-gu, Daejeon 34055, Republic of Korea*
[12]*University of Science and Technology, Korea (UST), 217 Gajeong-ro,Yuseong-gu, Daejeon 34113, Republic of Korea*
[13]*School of Physics and Astronomy, Sun Yat-sen University, 2 Daxue Road, Zhuhai, Guangdong 519082, People's Republic of China*
[14]*Yunnan Observatories, Chinese Academy of Sciences, 396 Yangfangwang, Guandu District, Kunming 650216, People's Republic of China*
[15]*Chinese Academy of Sciences, South America Center for Astronomy, National Astronomical Observatories, CAS, Beijing 100101, People's Republic of China*
[16]*Institute of Astronomy and Astrophysics, Academia Sinica, 11F of Astronomy-Mathematics Building, AS/NTU No. 1, Section 4, Roosevelt Road., Taipei 10617, Taiwan*
[17]*School of Space Research, Kyung Hee University, Yongin-Si, Gyeonggi-Do 17104, Republic of Korea*
[18]*Kavli Institute for Astronomy and Astrophysics, Peking University, 5 Yiheyuan Road, Haidian District, Beijing 100871, People's Republic of China*
[19]*Department of Physics, Anhui Normal University, Wuhu, Anhui 241002, People's Republic of China*
[20]*Institute of Astrophysics, School of Physics and Electronical Science, Chuxiong Normal University, Chuxiong 675000, People's Republic of China*
[21]*Institute of Astronomy and Astrophysics, Anqing Normal University, Anqing 246133, People's Republic of China*
[22]*College of Science, Yunnan Agricultural University, Kunming 650201, People's Republic of China*
[23]*S. N. Bose National Centre for Basic Sciences, Block-JD, Sector-III, Salt Lake City, Kolkata 700106, India*
[24]*Physical Research Laboratory, Navrangpura, Ahmedabad 380 009, India*
[25]*Indian Institute of Space Science and Technology, Thiruvananthapuram 695 547, India*

This paper has been typeset from a TEX/LATEX file prepared by the author.